*Characterization and Application of Nanomaterials (2023) Volume 6 Issue 2*
doi:10.24294/can.v6i2.3665

ORIGINAL RESEARCH ARTICLE

# Synthesis of vanadium oxide nanoparticles/Psi heterojunction photodetector

**Maysoon H. Ismail[1,*], Alaa H. Ali[1], Sabah M. Thahab[2]**

[1] *Department of Electrical Engineering, University of Technology, Iraq, Baghdad 10066, Iraq*

[2] *Nanotechnology and Advanced Materials Research Unit (NAMRU), Faculty of Engineering, University of Kufa, Kufa 540011, Najaf, Iraq*

*** Corresponding author:** Maysoon H. Ismail, eee.19.03@grad.uotechnology.edu.iq

## ABSTRACT

Nanoparticle $V_2O_5$ is prepared by the measurement of X-ray diffraction (XRD) and atomic force microscopy (AFM) analyses. The crystallite size = 19.59 nm, optical energy gap = 2.6 eV, an average particle size of 29.58 nm and, RMS roughness of ~6.8 nm. Also, Fourier transformer infrared spectrophotometer (FTIR) showed a porous free morphology with homogeneity and uniformity on the sample surface. The film surface exhibited no apparent cracking and, the grains exhibited large nicely separated conical columnar growth combined grains throughout the surface with coalescence of some columnar grains at a few places. The fabrication of a thin film of $V_2O_5$ NPs/PSi heterojunction photodetector was characterized and investigated.

***Keywords:*** $V_2O_5$; nanoparticles; porous silicon; AFM; XRD; heterojunction photodetector

**ARTICLE INFO**

Received: 13 November 2023
Accepted: 14 December 2023
Available online: 22 December 2023



## 1. Introduction

Numerous fields could greatly benefit from nanotechnology. By creating brand-new approaches to resolving environmental issues, nanomaterials have the potential to enhance the environment. The potential for nanotechnology to overcome the chemical and physical constraints of materials comprised of microparticles has been widely acknowledged. An important class of materials used in a variety of industrial applications, vanadium oxides exhibit an intriguing and varied concern of chemical and physical properties due to diverse metal oxidation situations (from +II to +V) and V-O organization geometries. For more than 50 years, the theoretical and experimental condensed matter and materials communities have researched vanadium oxygen structures ($V_2O_5$, $VO_2$), a sample of powerfully associated resources[1,2].

In comparison to other vanadium oxides, Vanadium Pentoxide ($V_2O_5$) has good electrical and chemical properties, making it a possible contender for electronic applications[3]. According to studies, $V_2O_5$ is used to make field effect transistors (FET), chemical sensors, energy harvesters, and other devices[4,5]. Also, it is a great option for optoelectronic applications like photo-detectors due to its direct bandgap of 2.2 eV to 2.7 eV which has been the subject of a great deal of fundamental research[6,7].

Metal-semiconductor transition, which is distinguished by a sudden

shift in optical and electrical properties, has been demonstrated to exhibit a variety of chromogenic properties, including vanadium pentoxide elements used for solar cells and transmittance modification in smart windows, and the technological features of conversion metal oxides have been the focus of study in the latest years among a variety of oxygen-containing compounds with various chemical, optical, and structural characteristics phases including VO, $VO_2$, $V_2O_3$, and $V_2O_5$ exhibit significant changes in their properties depending on their structural makeup, which also affects other characteristics[8–11].

Several systems of vanadium oxides may be created via altering the statement development factors otherwise through post-process management, such as added annealing[12,13]. In terms of applications, the maximum exciting vanadium oxides are $VO_2$ and $V_2O_5$. It's an ideal applicant for thermochroic coverings according to the modification from semiconducting to semimetal properties approximately of 68 °C and $V_2O_5$, made an object of several theoretical and applied studies, due to their industrial importance for many technological applications.

Moreover, vanadium pentoxide ($V_2O_5$) is a thermodynamically steady system, which displays electrochromic properties. $V_2O_5$ thin films can be used in optical filters, reflectance mirrors, as well as surfaces with tunable emittance for temperature mechanism control of space vehicles[14,15]. The aim of this study was to focus on the preparation of $V_2O_5$ NPs by hydrothermal method and study the structural, topographical and optical properties to reach the optimum condition in manufacturing the photodetector.

## 2. Experimental part

### 2.1. Prepared of $V_2O_5$ nanoparticles

The hydrothermal method refers to material preparation by chemical reaction to facile the controlling of the reaction parameters such as temperature and reaction time to obtain highly homogeneous products.

$V_2O_5$ NPs synthesized, where 1.8 g powder of material was added into 100 mL of distilled water, and the solution was placed on a magnetic stirrer for 15 min at 50 °C, after cooling to room temperature, the addition of 1 g of polymethyl methacrylate (PMMA) to 50 mL of Acetone at various concentrations of materials (1:9, 1.5:8.5 and 2:8) at the first step and 2 g of PMMA at the second stage.

### 2.2. Fabrication of porous silicon

In the etching process, a Teflon container was used because it does not react with HF, which has a very offensive nature. The etching cell consisted of two, upper and lower parts, and the Si pieces steadied between them, as shown in **Figure 1**. The upper part contained a circular cavity in the center to keep the etchant and it provided with an O-ring to prevent the etchant from leaking. The edge of the lower part formed as a screw to relate the parts together. Porous silicone was created by photo electrochemical etching approach, the surface of a Si wafer using a combination of hydrofluoric acid 45% and 100% ethanol, and then placing the wafer in the bottom of Teflon cells in a ratio of 1:1, an Au ring was used as an electrode with a current density of 15 $mA \cdot cm^{-2}$ to generate an etched area of the sample of (0.785) $cm^2$.

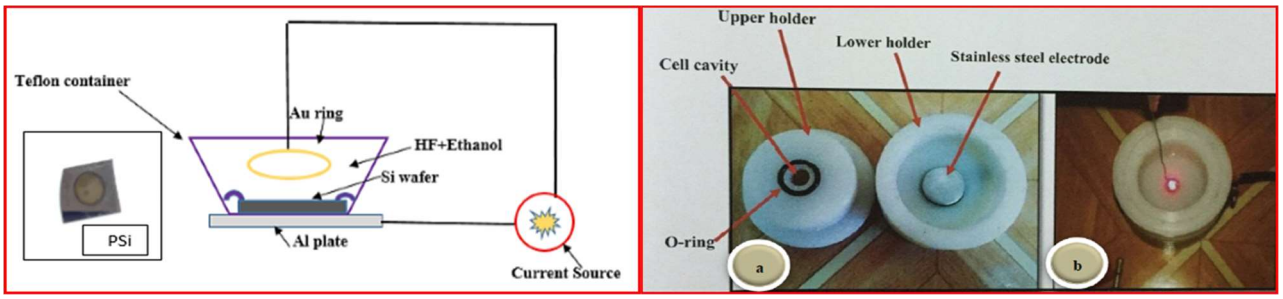


**Figure 1.** Schematic of etching cell and processing.

### 2.3. Thin film deposition by drop casting method

Glass slides of 1.50 × 1.50 $cm^2$ area, were used as a substrate. They were cleaned with alcohol in an ultrasonic bath in order to remove the impurities and residuals from their surface. Then, four drops of the colloidal were used in preparing the $V_2O_5$ thin film using a specific syringe (YE3K061872:10100ML).

This process begins with depositing the droplets of $V_2O_5$ via syringe in a certain amount on the glass sample, which is then heated to dry for 20 min. **Figure 2** shows the X-ray diffraction analysis of $V_2O_5$. The shape and size of $V_2O_5$ nanoparticles were investigated by using AFM (AA 3000 Scanning Probe Microscope). The analysis from X-ray diffraction when $V_2O_5$ NPs that deposited on a glass substrate by drop casting method at 80 ℃. It notes that the sample has a polycrystalline structure, with 7 peaks in the diffraction spectrum which are (110), (200), (001), (101), (400), (411) and (600).

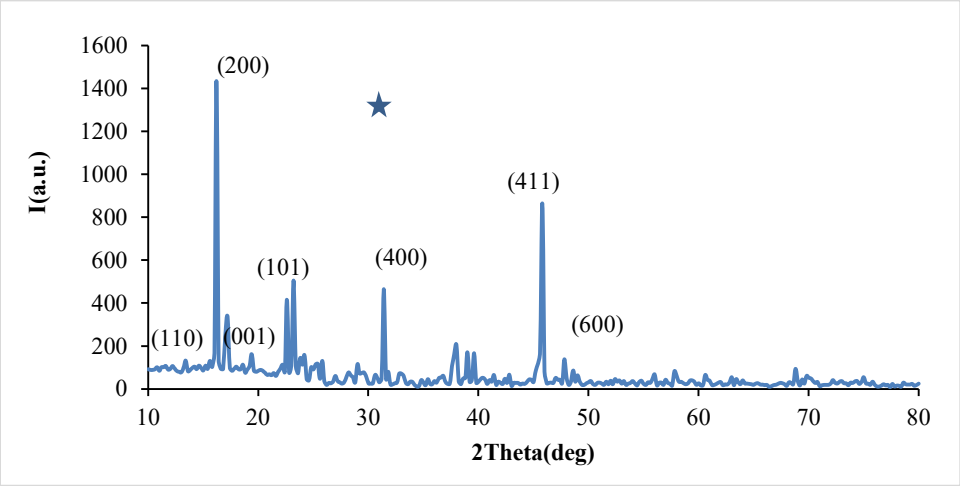


**Figure 2.** XRD diffraction of $V_2O_5$ nanostructure.

## 3. Results and discussions

### 3.1. Structural properties

The structural properties of the deposited thin film at room temperature were studied by using an X-ray diffractometer (XRD-6000, Shimadzu X-ray Diffractometer). The optical absorption of the colloidal $V_2O_5$ NPs was measured using a spectrophotometer (CARY, 100 CONC plus, UV-Vis-NIR, Splitbeam Optics, Dual detectors) in the range of 350–1100 nm, using a quartz vessel.

The crystallite size values of $V_2O_5$ were calculated by measuring the half width of the peak maximum intensity (FWHM), and 2θ of the directions' peaks using formulae given by Equation (1). Scherer's equation is shown in **Table 1**. The strong and narrow peaks can be attributed to $V_2O_5$ preferential development along the (200) and (110) planes.

$$D = \frac{0.9\lambda}{BCos\theta} \quad (1)$$

The average crystallite size (D), which can be estimated using Scherrer's formulae; $\lambda$ is the wavelength of CuK$\alpha$ (= 1.5405 Å), $B$ is the full width at half maximum (FWHM). The FWHM of the preferred orientation (peak) could be measured since it is equal to the width of the line profile (in radian) at the half of the maximum intensity; and $\theta$ is Bragg's diffraction angle. The single line method is one of the several line profile analysis methods based on a Voigt function to determine the size–strain parameters (microstrains and crystallite sizes) was computed strain (η) and dislocation density (σ) as shown in **Table 1**.

**Table 1.** Summary of XRD characterization for $V_2O_5$ powder.

| Crystalline size (nm) | $\delta \times 10^{14}$ lines·m$^{-2}$ | $\eta \times 10^{-4}$ lines$^{-2}$·m$^{-4}$ |
|---|---|---|
| 29.24 | 11.84 | 11.69 |
| 30.46 | 11.37 | 10.77 |
| 14.91 | 23.22 | 44.92 |
| 16.24 | 21.32 | 37.89 |
| 16.80 | 20.61 | 35.40 |
| 21.82 | 15.87 | 20.99 |

**Figure 3** shows the 3D AFM micrographs and histograms of $V_2O_5$. The atomic force microscopy analysis showed a porous free morphology with homogeneity and uniformity on the sample surface. There was no visible breaking on the film's surface. The grains had huge beautifully separated conical columnar development joined grains all over the surface, with some columnar grains coalescing in a few locations. It had an average particle size of 29.58 nm and an RMS roughness of 6.8 nm. It should be noted that significant sample roughness is essential for photovoltaic applications since rough surfaces have a substantially larger total surface area than smooth surfaces.

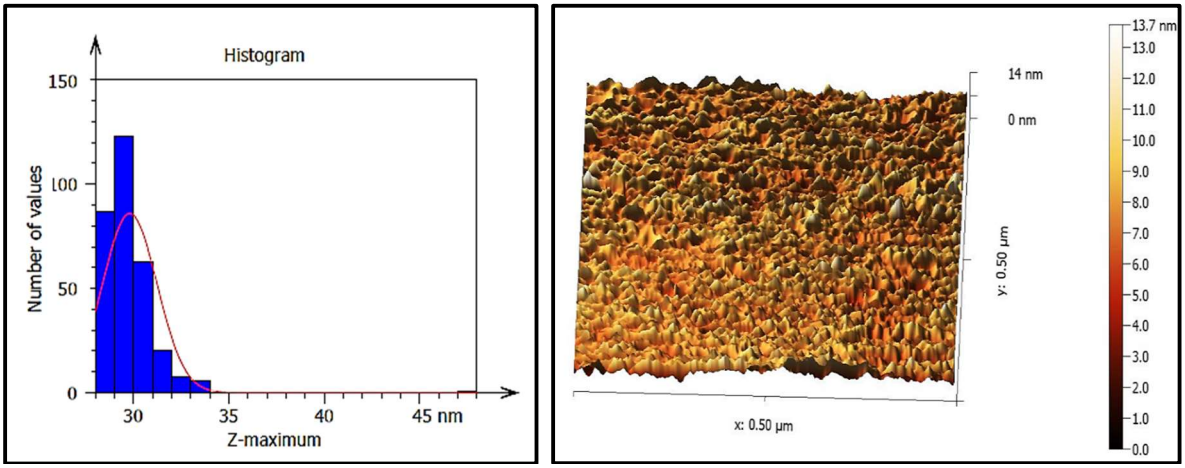


**Figure 3.** AFM image histogram of $V_2O_5$.

**Figure 4** shows FTIR spectra of $V_2O_5$ were analyzed in the range of 450–4500 cm$^{-1}$ wave number that identifies the chemical bonds and functional sets in the composite. The large broad band at 3450 and 3431 cm$^{-1}$ is ascribed to the O-H. The peak at 3000 and 2928 cm$^{-1}$ for C-H groups. The absorption at 2362 and 2358 cm$^{-1}$ is ascribed to the C=C bond. The peaks at 1652, 1655, 1658 and 1617 cm$^{-1}$ are due to vibration of C=O, N-O and C=C, respectively.

While the peaks at 1457, 1143, 1138 and 1056 cm$^{-1}$ are ascribed to the C=H, C-N and C-O, respectively. $V_2O_5$ FTIR spectra revealed three distinct vibration styles: V=O feelings at 975 cm$^{-1}$, V-O V symmetric stretch around 500 and 540 cm$^{-1}$, and V-O-V asymmetric bounce at 770 cm$^{-1}$. The bands perceived between 950 and 1020 cm$^{-1}$ were unambiguously ascribed to stretching modes (V-O). The bridge V-O-V stretching was assigned bands between 700 and 900 cm$^{-1}$.

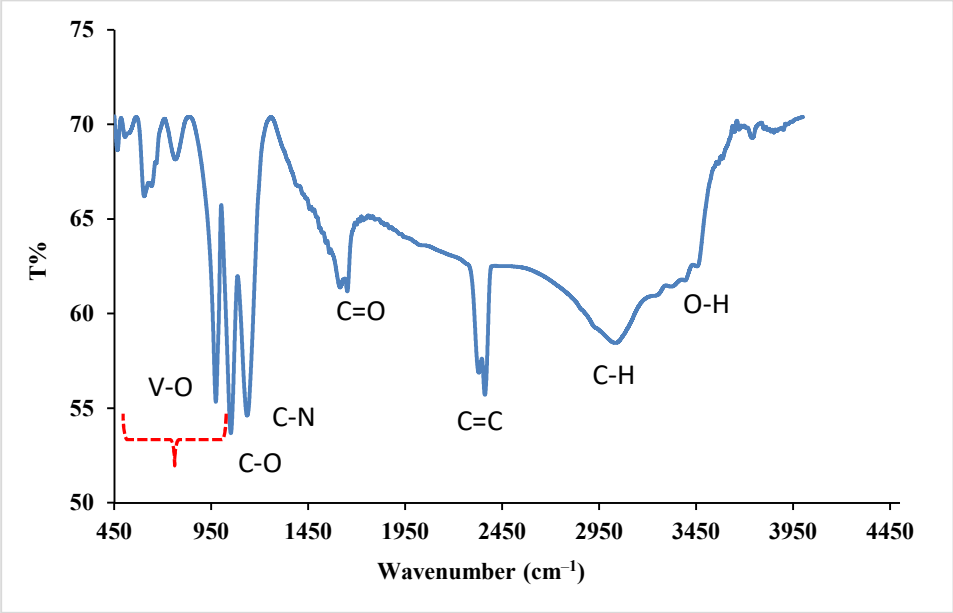


**Figure 4.** FTI R of $V_2O_5$ NPs.

## 3.2. Optical property

The band gap of $V_2O_5$ NPs is shown in **Figure 5** as a plot of $(\alpha h\upsilon)^2$ versus photon energy hυ (where α is the absorption coefficient). The energy of the band gap was calculated using the Tauc relation as in Equation (2). The band gap of $V_2O_5$ NPs was discovered to be 2.6 eV by projecting the linear component of the curve toward the photon energy axis.

$$(\alpha h\nu) = A(h\nu - Eg) \quad (2)$$

where A is the absorption coefficient;

hν is the Photon energy;

Eg is the energy of the band gap, for direct band gap n = 1/2. A photoluminescence (PL) research at room temperature was performed to explore the optical characteristics of $V_2O_5$ that was drop cast onto a glass substrate. **Figure 6** depicts the PL spectra. The emission peak, which was locked at around 476 nm, revealed that the luminescence is connected to band edge recombination in $V_2O_5$ thin film. This agrees with the optical features of the samples, where the energy gap was 2.6 eV.

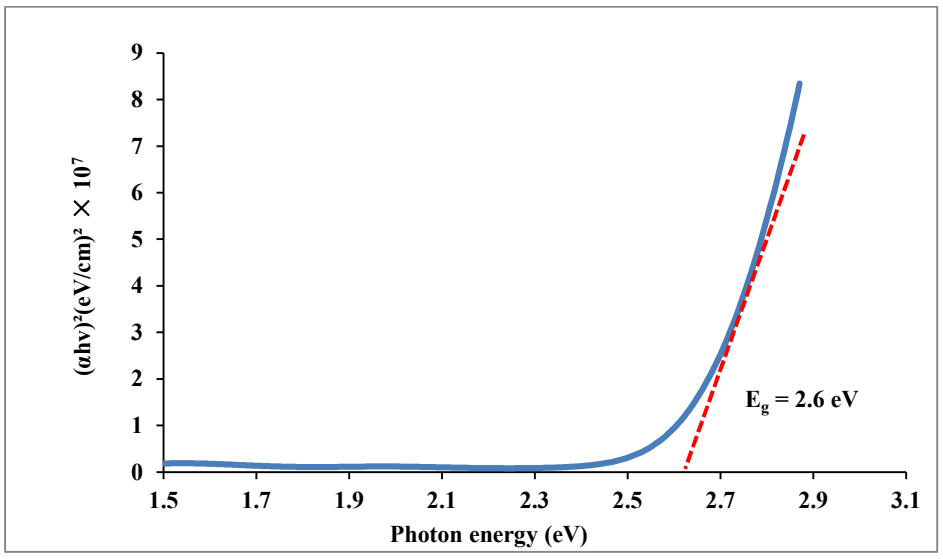


**Figure 5.** Tauc's plot of $V_2O_5$ NPs.

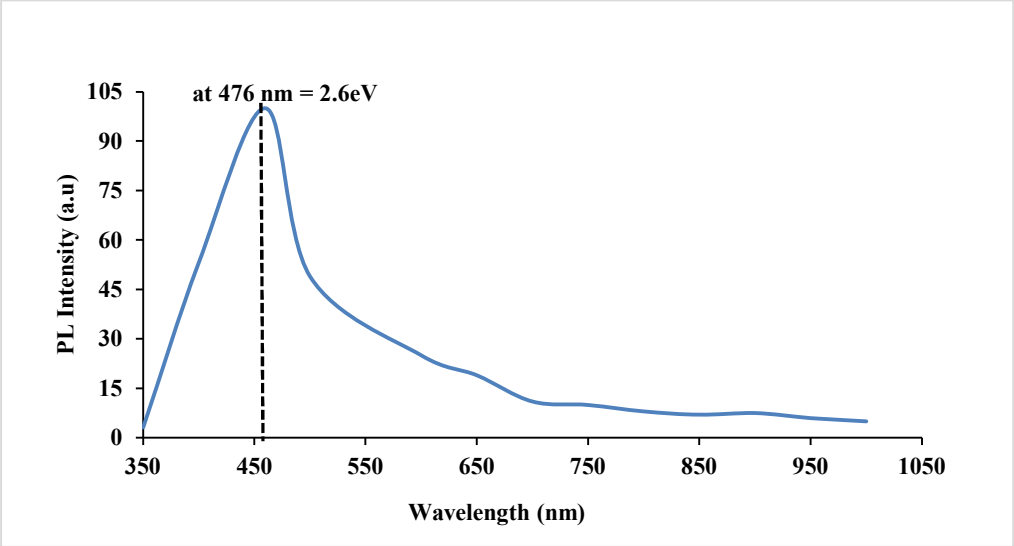


**Figure 6.** PL spectrum of $V_2O_5$ thin film.

### 3.3. Ag/$V_2O_5$/PSi/n-Si/Ag heterojunction characterizations

$V_2O_5$/PSi/n-Si/ heterojunction photodetector consists of two layers. The first place of junction is between the $V_2O_5$ layer and porous silicon (PSi) and the second place of junction is made up between the porous silicon layer and crystalline (substrate) silicon (PSi/n-Si), so there are two depletions regions as shown in **Figure 7**. All samples are made up of the diverse concentrations of (1:9, 1.5:8.5 and 2:8) once with 1 g and the second stage with 2 g.

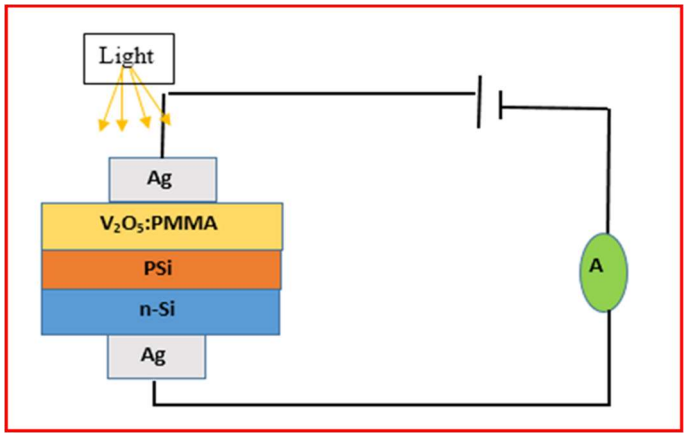


**Figure 7**. Diagram of detector connection circuit Ag/$V_2O_5$/PSi/n-Si/Ag heterojunction photodetector.

#### 3.3.1. Responsivity

The responsivity of structures was examined in the wavelength range of 350–1000 nm with 3V bias and it is calculated by Equation (3).

$$R_\lambda = \frac{I_{Ph}}{P_{in}} (\text{A/W}) \quad (3)$$

where $I_{ph}$ *is* the photocurrent, and $P_{in}$ is the input power.

**Figure 8** depicts the responsivity plots as a function of the wavelength of $V_2O_5$/PSi/n-Si structures generated at various concentrations (1:9, 1.5:8.5, and 2:8) with 1 g PMMA:Acetone. The responsivity curve of $V_2O_5$/PSi/n-Si is observed to have three response peaks; the first peak is located at 440–550 nm due to the absorption edge of $V_2O_5$ nanoparticles, the second region is located at 700–750 nm, due to the absorption edge of PSi, and the third peak is located at 800–850 nm due to the absorption edge of silicon.

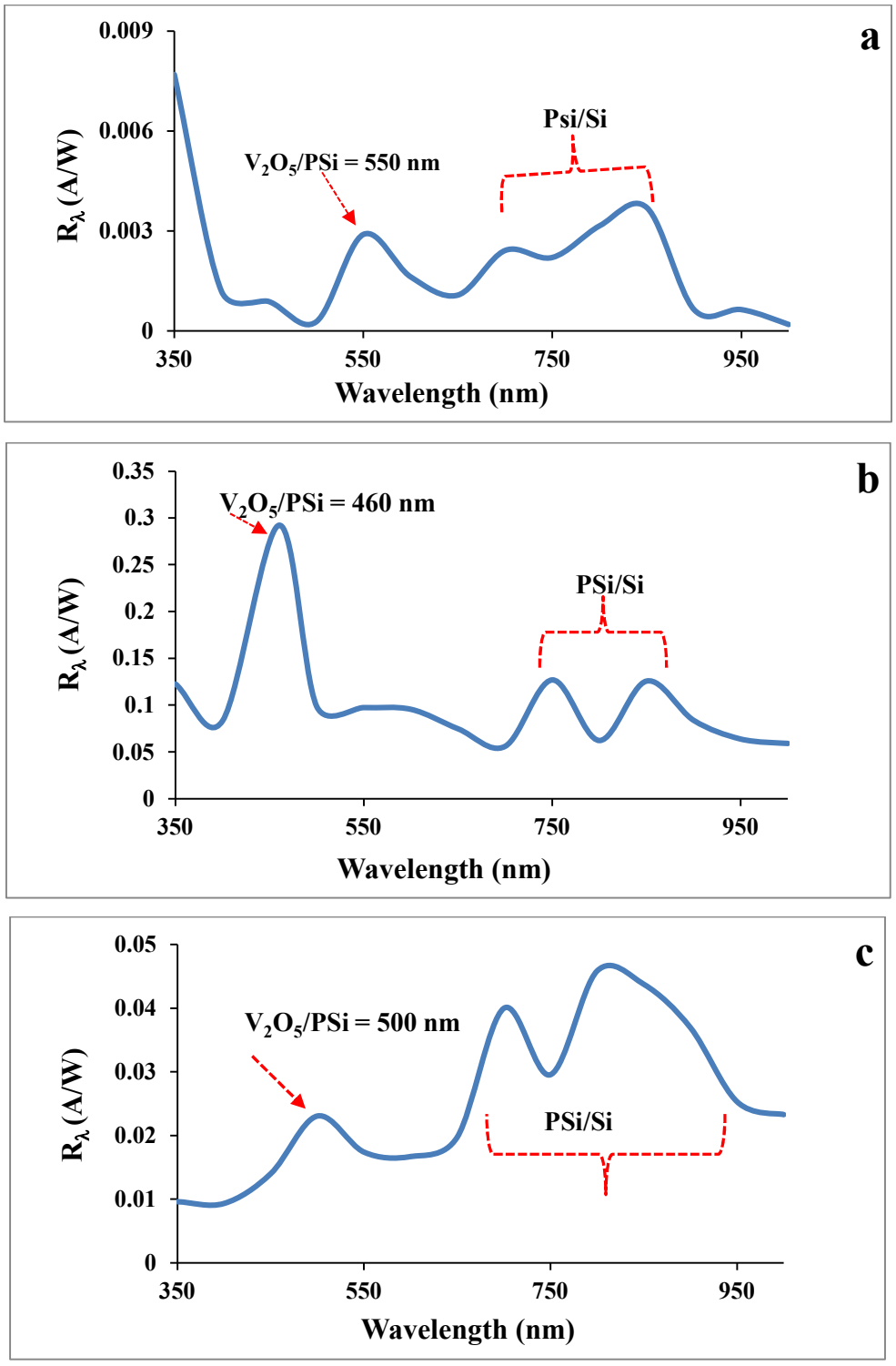


**Figure 8.** Responsivity as a function of wavelength of $V_2O_5$/PSi/ n-Si photo-detectors with different concentrations (1:9, 1.5:8.5 and 2:8) with 1 g PMMA:Acetone.

### 3.3.2. Detectivity

The detectivity is an important metric for Photo-detectors since it represents a minimum detectable power; hence, the detector's performance is associated with this value. The specific detectivity as a function of wavelength for $V_2O_5$/PSi/n-Si Photo-detectors at different concentrations (1:9, 1.5:8.5, and 2:8) with 1 g PMMA:Acetone. **Figure 9** shows the detectivity curve consists of two peaks; the first peak is situated in the visible area, while the second region is located in the NIR region.

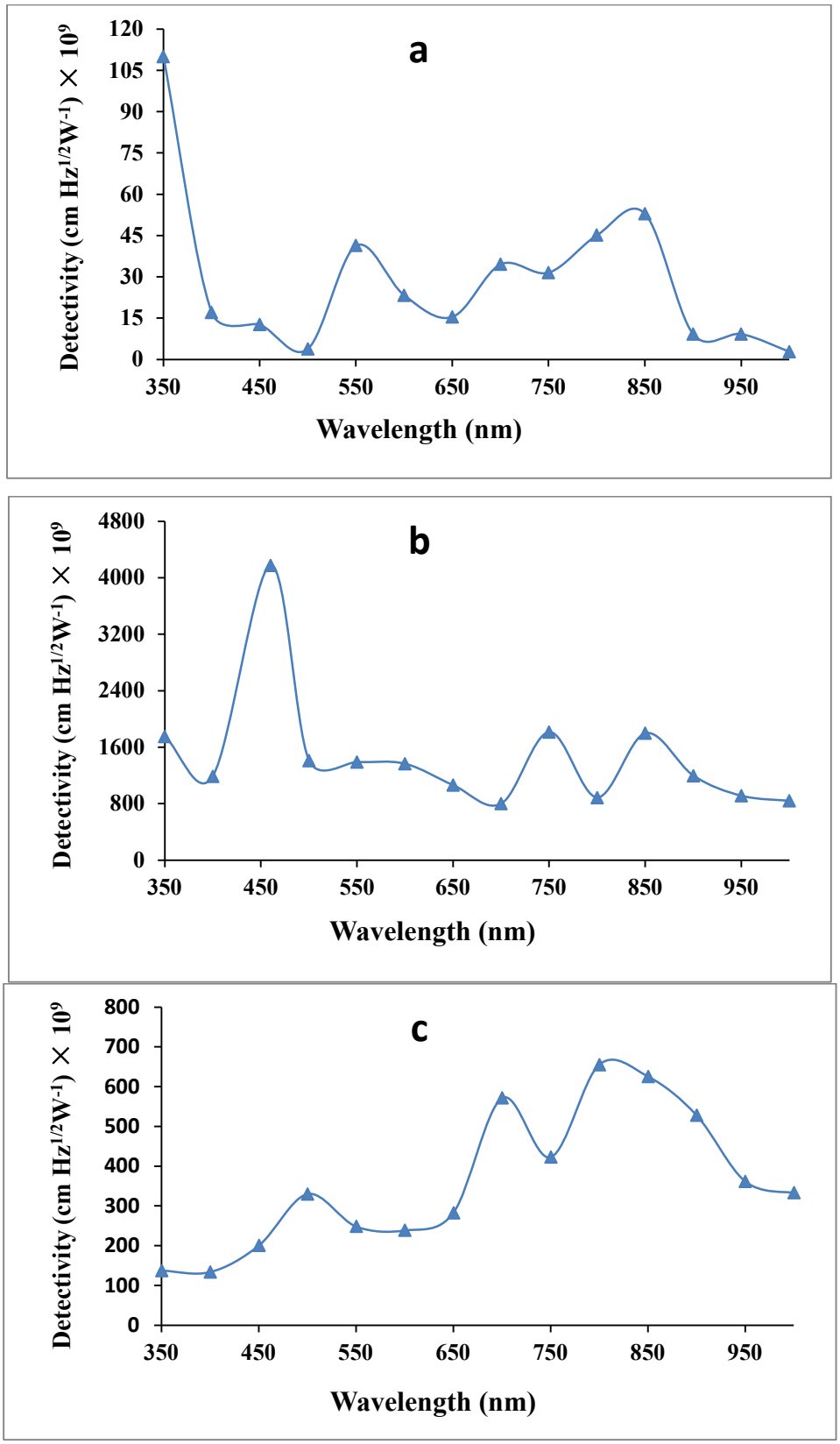


**Figure 9.** Detectivity plots for $V_2O_5$/PSi/n-Si Photo-detectors respectively at different concentrations (1:9, 1.5:8.5 and 2:8) with 1 g PMMA:Aceton.

$$D* = R_\lambda \frac{\sqrt{A.\Delta f}}{I_n} \tag{4}$$

$$I_n = (2qI_d\Delta f)^{\frac{1}{2}} \quad (5)$$

where $\Delta f$ is the bandwidth, $A$ is active area of the detector, $I_d$ is dark current and $q$ is electron charge. The maximal D* for sample was determined to be 4.1 × $10^{12}$ $W^{-1}$·cm·$Hz^{1/2}$ at 460 nm (b).

### 3.3.3. Carrier lifetime

Circuit Voltage Decay OCVD is a fundamental parameter for a metal-insulator transition (MIT) material industry which influences the performances of the device. The lifetime is a free path for the charge carriers providing the time required for both the hole current and the electron current to generate the necessary current. Time is calculated from the inverse of the frequency. The forward current flows through the device, then the circuit is abruptly opened and forward voltage drop decay is measured.

The accuracy of the OCVD measurement depends on the precision of the oscilloscope, the temperature measurement and the affected noise. **Figure 10** represents images for the lifetime for $V_2O_5$/PSi/n-Si at different concentrations (1:9, 1.5:8.5 and 2:8) with 1 g PMMA:Acetone and the value of the time calculated as shown in **Table 2**.

**(a)** **(b)** **(c)**

**Figure 10.** The lifetime of structure $V_2O_5$/PSi/n-Si with different concentrations (1:9, 1.5:8.5 and 2:8) with 1 g PMMA:Acetone.

**Table 2.** Lifetime of structure $V_2O_5$/PSi/n-Si with different conditions.

| Number | Samples | Lifetimes (msec) |
|---|---|---|
| a | 1:9<br>PMMA:Acetone<br>1 g | 7.1 |
| b | 1.5:8.5<br>PMMA:Acetone<br>1 g | 12.5 |
| c | 2:8<br>PMMA:Acetone<br>1 g | 3.6 |

## 3.4. Statistical analysis and experimental results of Ag/$V_2O_5$/PSi/n-Si/Ag

Statistical analyses have been achieved by SPSS 24.0 window using Least Significant Difference (LSD) between variables means to calculate a significant variation among all samples of $V_2O_5$/PSi/n-Si with different concentrations (1:9, 1.5:8.5 and 2:8) with three samples of 1 g and, three samples with 2 g of PMMA:Acetone. LSD Analysis is defined as particular two values at levels of statistical probability indicated as the statistically significant function at α = 0.05 level and significant at α = 0.0l level. The analysis of the experimental results showed that there are significant differences between the variable of the samples S and the variable wavelengths λ which affect the variable of responsivity R of the light to the material, as shown in **Table 3**, and the effect of S and λ on efficiency Q of the system as shown in **Table 4**, also, the effect of S and λ on important parameter of detectivity D as shown in **Table 5**.

In addition, there is a correlation between the parameters of the system, as shown in **Table 6**, where the coefficient of correlation (r = 1). There is a very strong positive relationship between the two variables of the parameters, and also concerning the symbol **Sig**, which means that there is a statistically significant function between the parameters. For example, the value between two parameters, wavelength and efficiency is Sig = 0.035, which is less than α value, if compared when the value is at the level α = 0.05, which means that this is an accepted value with a large statistically significant function and the percentage of error is small. While for the level α = 0.01, there is a very strong positive relationship and the rate of error percentage in this experimental work is externally small.

**Table 3.** Effect of S and λ on responsivity.

| **λ (nm)** | **S** | | | | | | **Mean of (λ)** |
|---|---|---|---|---|---|---|---|
| | **S1** | **S2** | **S3** | **S4** | **S5** | **S6** | |
| 350 | 0.0077 | 0.1227 | 0.0096 | 0.0077 | 0.0096 | 0.0402 | **0.0329** |
| 400 | 0.0012 | 0.0833 | 0.0094 | 0.0075 | 0.0110 | 0.0337 | **0.0244** |
| 450 | 0.0009 | 0.2923 | 0.0140 | 0.0091 | 0.0126 | 0.1202 | **0.0749** |
| 500 | 0.0003 | 0.0988 | 0.0231 | 0.0069 | 0.0081 | 0.0421 | **0.0299** |
| 550 | 0.0029 | 0.0974 | 0.0174 | 0.0066 | 0.0061 | 0.0467 | **0.0295** |
| 600 | 0.0016 | 0.0957 | 0.0167 | 0.0067 | 0.0058 | 0.0437 | **0.0284** |
| 650 | 0.0011 | 0.0746 | 0.0198 | 0.0063 | 0.0054 | 0.0523 | **0.0266** |
| 700 | 0.0024 | 0.0562 | 0.0400 | 0.0073 | 0.0084 | 0.1133 | **0.0379** |
| 750 | 0.0022 | 0.1271 | 0.0296 | 0.0068 | 0.0104 | 0.1144 | **0.0484** |
| 800 | 0.0032 | 0.0623 | 0.0458 | 0.0070 | 0.0088 | 0.1664 | **0.0489** |
| 850 | 0.0037 | 0.1259 | 0.0438 | 0.0076 | 0.0116 | 0.1433 | **0.0560** |
| 900 | 0.0006 | 0.0838 | 0.0370 | 0.0069 | 0.0077 | 0.1064 | **0.0404** |
| 950 | 0.0006 | 0.0640 | 0.0253 | 0.0068 | 0.0074 | 0.0890 | **0.0322** |
| 1000 | 0.0002 | 0.0590 | 0.0233 | 0.0067 | 0.0050 | 0.0890 | **0.0305** |
| Mean of S | **0.0020** | **0.1031** | **0.0253** | **0.0071** | **0.0084** | **0.0858** | |

LSD (0.05) for (S) = 0.0041,
LSD (0.05) for (λ) = 0.0029,
LSD (0.05) for (S × λ) = 0.052.

**Table 4.** Effect of S and λ on Q.

| **λ (nm)** | **S** | | | | | | **Mean of (λ)** |
|---|---|---|---|---|---|---|---|
| | **S1** | **S2** | **S3** | **S4** | **S5** | **S6** | |
| 350 | 2.725 | 43.468 | 3.407 | 2.725 | 3.407 | 14.240 | **11.6620** |
| 400 | 0.371 | 25.823 | 2.904 | 2.317 | 3.398 | 10.440 | **7.5422** |
| 450 | 0.245 | 78.783 | 3.866 | 2.525 | 3.479 | 33.868 | **20.4610** |
| 500 | 0.067 | 24.514 | 5.723 | 1.705 | 2.003 | 10.445 | **7.4095** |
| 550 | 0.652 | 21.953 | 3.923 | 1.499 | 1.367 | 10.535 | **6.6548** |
| 600 | 0.337 | 19.769 | 3.453 | 1.392 | 1.209 | 9.021 | **5.8635** |
| 650 | 0.206 | 14.239 | 3.774 | 1.201 | 1.029 | 9.979 | **5.0713** |
| 700 | 0.428 | 9.951 | 7.084 | 1.285 | 1.483 | 20.067 | **6.7163** |
| 750 | 0.365 | 21.011 | 4.891 | 1.119 | 1.722 | 18.910 | **8.0030** |
| 800 | 0.489 | 9.654 | 7.104 | 1.088 | 1.360 | 25.799 | **7.5823** |
| 850 | 0.540 | 18.370 | 6.382 | 1.114 | 1.688 | 20.903 | **8.1662** |
| 900 | 0.089 | 11.550 | 5.091 | 0.948 | 1.059 | 14.659 | **5.5660** |
| 950 | 0.084 | 8.352 | 3.302 | 0.890 | 0.971 | 11.622 | **4.2035** |
| 1000 | 0.025 | 7.319 | 2.891 | 0.830 | 0.615 | 11.041 | **3.7868** |
| Mean of S | **0.4731** | **22.4826** | **4.5568** | **1.4741** | **1.7707** | **15.8235** | |

LSD (0.05) for (S) = 0.297,
LSD (0.05) for (λ) = 1.889,
LSD (0.05) for (S × λ) = 2.115.

**Table 5**. Effect of S and λ on D.

| λ (nm) | S | | | | | | Mean of (λ) |
|---|---|---|---|---|---|---|---|
| | S1 | S2 | S3 | S4 | S5 | S6 | |
| | Mean × $10^{11}$ | | | | | | |
| 350 | 1.100 | 17.542 | 1.375 | 1.100 | 1.375 | 5.747 | **4.7065** |
| 400 | 0.171 | 11.910 | 1.339 | 1.068 | 1.567 | 4.815 | **3.4783** |
| 450 | 0.127 | 41.787 | 2.006 | 1.295 | 1.805 | 17.183 | **10.7005** |
| 500 | 0.038 | 14.133 | 3.299 | 0.983 | 1.155 | 6.022 | **4.2717** |
| 550 | 0.414 | 13.922 | 2.488 | 0.950 | 0.867 | 6.681 | **4.2203** |
| 600 | 0.233 | 13.677 | 2.389 | 0.963 | 0.836 | 6.241 | **4.0565** |
| 650 | 0.154 | 10.672 | 2.829 | 0.900 | 0.771 | 7.479 | **3.8008** |
| 700 | 0.346 | 8.032 | 5.718 | 1.037 | 1.197 | 16.197 | **5.4212** |
| 750 | 0.316 | 18.170 | 4.230 | 0.968 | 1.489 | 16.353 | **6.9210** |
| 800 | 0.452 | 8.905 | 6.553 | 1.003 | 1.254 | 23.798 | **6.9942** |
| 850 | 0.530 | 18.005 | 6.255 | 1.092 | 1.655 | 20.487 | **8.0040** |
| 900 | 0.092 | 11.986 | 5.284 | 0.984 | 1.099 | 15.213 | **5.7763** |
| 950 | 0.092 | 9.149 | 3.617 | 0.975 | 1.064 | 12.730 | **4.6045** |
| 1000 | 0.028 | 8.440 | 3.333 | 0.957 | 0.709 | 12.730 | **4.3662** |
| Mean of S | **0.292** | **14.738** | **3.623** | **1.020** | **1.203** | **12.263** | |

LSD (0.05) for (S) = 0.899,
LSD (0.05) for (λ) = 1.275,
LSD (0.05) for (S × λ) = 2.33.

**Table 6.** Correlation among parameters.

| | | R | Q | D |
|---|---|---|---|---|
| Wavelength | **R** | 0.050 | –0.567* | 0.051 |
| | **Sig.** | 0.865 | 0.035 | 0.862 |
| R | **R** | 1 | 0.746** | 1.000** |
| | **Sig.** | | 0.002 | 0.000 |
| Q | **R** | | 1 | 0.746** |
| | **Sig.** | | | 0.002 |

*. Correlation is significant at the 0.05 level (2-tailed).
**. Correlation is significant at the 0.01 level (2-tailed).

## 4. Conclusion

In conclusion, this work demonstrated how to create $V_2O_5$ thin films to manufacture and characterize heterojunction photodetector used in electronic systems. According to XRD and AFM analyses, the pictures show that considerable roughness of the sample is necessary for photovoltaic applications was concluded since the total surface area is substantially larger when the surface is rough than when the surface is smooth. Due to the good Photo-detector performance, the method employed has been confirmed by the findings of responsivity in the visible and near infrared regions, where this approach is used to construct silicon photodetectors for detecting a low optical signal power with ultra-small size and low cost.

## Author contributions

Dr. Sabah M. Thahab conceived the experiments. Dr. Sabah M. Thahab and Dr. Alaa H. Ali planned and supervised the project. Dr Maysoon H. Ismail carried out the experiments. Dr. Alaa H. Ali and Dr. Maysoon H. Ismail contributed to samples preparation. Dr. Maysoon H. Ismail contributed to the interpretation of the results and took the lead in writing the manuscript. All authors provided critical feedback and helped shape the research, analysis and manuscript.

## Conflict of interest

The authors declare that they have no conflicts of interest.

# References


1. Ismail MH, Ali AH, Thahab SM. Fabrication and characterization of a $VO_2$:PVP/PSi/ and n-Si heterojunction for photodetector applications. *Optics Continuum* 2023; 2(6): 1301–1314. doi: 10.1364/OPTCON.484653
2. Chuah R, Gopinath SCB, Anbu P, et al. Synthesis and characterization of reduced graphene oxide using the aqueous extract of *Eclipta prostrata. 3 Biotech* 2020; 10: 364. doi: 10.1007/s13205-020-02365-4
3. Ramanathan S, Gopinath SCB, Md Arshad MK, et al. Aluminosilicate nano-composites from incinerated Chinese holy joss fly ash: A potential nanocarrier for drug cargos. *Scientific Reports* 2020; 10: 3351. doi: 10.1038/s41598-020-60208-x
4. Markov A, Greben K, Mayer D, et al. In situ analysis of the growth and dielectric properties of organic self-assembled monolayers: A way to tailor organic layers for electronic applications. *ACS Applied Materials & Interfaces* 2016; 8(25): 16451–16456. doi: 10.1021/acsami.6b04021
5. Sahatiya P, Reddy K CS, Badhulika S. Discretely distributed 1D $V_2O_5$ nanowires over 2D $MoS_2$ nanoflakes for an enhanced broadband flexible photodetector covering the ultraviolet to near infrared region. *Journal of Materials Chemistry C* 2017; 5(48): 12728–12736. doi: 10.1039/C7TC05036D
6. Khandaker JI, Tokuda M, Ogata Y, et al. Formation of vanadium oxide (V-O system) graded compounds under strong gravitational field. *Defect and Diffusion Forum* 2015; 363: 164–170. doi: 10.4028/www.scientific.net/DDF.363.164
7. Vijayakumar Y, Jyothi DS, Nagaraju P, Reddy MV. Structural, electrical and optical properties of spray deposited $V_2O_5$ thin films on glass substrates. *Physics and Chemistry of Glasses-European Journal of Glass Science and Technology Part B* 2016; 57(1): 37–41. doi: 10.13036/17533562.57.1.019
8. McNamara K, Tofail SAM. Nanoparticle in biomedical applications. Advances in Physics: X 2017; 2(1): 54–88. doi: 10.1080/23746149.2016.1254570
9. Uda MNA, Gopinath SCB, Hasim U, et al. Production and characterization of silica nanoparticles from fly ash: Conversion of agro-waste into resource. *Preparative Biochemistry & Biotechnology* 2021; 51(1): 86–95. doi: 10.1080/10826068.2020.1793174
10. Yan LP, Gopinath SCP, Anbu P, et al. Characterization and anti-bacterial potential of iron oxide nanoparticle processed eco-friendly by plant extract. *Preparative Biochemistry & Biotechnology* 2020; 50(10): 1053–1062. doi: 10.1080/10826068.2020.1783678
11. Shafeeq KM, Athira VP, Raj Kishor CH, Aneesh PM. Structural and optical properties of $V_2O_5$ nanostructures grown by thermal decomposition technique. *Applied Physics A* 2020; 126: 586. doi: 10.1007/s00339-020-03770-5
12. Osamah S, Alwahib AA, Fakhri MA. Study of single and symmetrical D-shaped optical fiber sensor based on gold nanorods. *Journal of Optics* 2023; 52: 2048–2058. doi: 10.1007/s12596-023-01119-8
13. Schneider K. Optical properties and electronic structure of $V_2O_5$, $V_2O_3$ and $VO_2$. *Journal of Materials Science: Materials in Electronics* 2020; 31: 10478–10488. doi: 10.1007/s10854-020-03596-0
14. Sieradzka K, Wojcieszak D, Kaczmarek D, et al. Structural and optical properties of vanadium oxides prepared by microwave-assisted reactive magnetron sputtering. *Optica Applicata* 2011; 9(2): 463–469.
15. Sorifi S, Moun M, Kaushik S, Singh R. High-temperature performance of a GaSe nanosheet-based broadband photodetector. *ACS Applied Electronic Materials* 2020; 2(3): 670–676. doi: 10.1021/acsaelm.9b00770